Research Article

Image Mosaic Algorithm-Based Analysis of Effects of Low-Dose X-Rays on Blood Immune Cells

Xiaohua Fu ,[1] Fei Miao ,[2] Jianbin Guo ,[2] Weijuan He ,[1] Yuying Deng ,[2] Yushan Wang ,[1] Xiaxiang Zeng ,[1] Wenbing Wang ,[2] and Yunfeng Liu [3]

[1]*Department of Interventional Therapy, Zhujiang Hospital of Southern Medical University, Guangzhou 510282, Guangdong, China*

[2]*Department of Cardiovascular Medicine, Zhujiang Hospital of Southern Medical University, Guangzhou 510282, Guangdong, China*

[3]*Department of Cardiovascular Medicine, Shenzhen Hospital of Southern Medical University, Shenzhen 518101, China*

Correspondence should be addressed to Xiaohua Fu; fuxiaohua@m.fafu.edu.cn

This work aimed to explore the effects of image mosaic algorithm- (IMA-) based low-dose X-rays on deoxyribonucleic acid (DNA) damage of peripheral blood lymphocytes in cardiovascular patients. 84 patients with interventional cardiovascular surgeries were selected as the research objects and divided into coronary intervention surgery (A) group, coronary angiography (B) group, radiofrequency ablation (C) group, and permanent cardiac pacemaker implantation (D) group. They were treated with IMA-based low-dose X-rays, DNA damage indicators of lymphocytes were detected, and the relationship was analyzed between those indicators and radiation dose. Results showed that the cumulative dose (CD) and dose area product (DAP) of group A were the lowest, and those of group D were obviously higher than those of the other three groups ($P < 0.01$). Besides, the results also showed that the values of CD and DAP of patients from group A and group D were 0.38 ± 0.08 (Gy) and 0.38 ± 0.08 (Gy/cm^2) and 1.37 ± 0.21 (Gy) and 1.37 ± 0.21 (Gy/cm^2), respectively. The comet tail DNA content (TDNA) and tail moment (TM) of each group after surgery increased dramatically compared with before surgery ($P < 0.01$), and the TDNA and TM of group D were greatly higher than those of the other three groups ($P < 0.01$). Therefore, TDNA and TM were markedly positively correlated with DAP and CD ($P < 0.01$). IMA-based X-ray radiotherapy caused reliable DNA damage to peripheral blood lymphocytes of cardiovascular patients, and the greater the radiation dose, the more serious the DNA damage.

1. Introduction

With the acceleration of the aging process and the improvement of living standards, the incidence of cardiovascular diseases continues to increase. Cardiovascular intervention is featured with simple operation, low risk of trauma, and short hospital stay, so it is widely applied in the clinical treatment of cardiovascular diseases [1, 2]. Cardiovascular intervention is a common method of diagnosis and treatment for cardiovascular diseases, which can sharply reduce the mortality of patients with cardiovascular diseases and also has an obvious effect on the quality of life of patients [3]. Interventional surgery is generally performed under the

guidance of X-ray fluoroscopy, and exposure is required for at least 5 minutes, usually about half an hour. During this process, both the physician and the patient will be damaged by high-dose ionizing radiation. Compared with physicians, patients do not have any protective measures, so the radiation exposure to patient is more harmful. X-ray is a low linear energy transfer ray, which is less harmful to the human body compared with other medical rays [4, 5]. Various organs and tissues in the human body have different sensitivities to ionizing radiation. Hematopoietic lymphoid tissue and vascular lymphatic endothelial cells belong to the highly and moderately sensitive tissues in turn. DNA sensitivity of cellular molecules is greater than that of

ribonucleic acid (RNA) and protein. Radiation can cause damage to the base, the breaking of hydrogen bond, the breaking of DNA single and double strands, and the loss of protein enzyme activity [6]. Besides, DNA is the main target molecule of the radiation effect, and the application of DNA damage as a biological dose evaluation indicator can more accurately evaluate the random effects of radiation.

X-ray projection technology has the characteristics of wide projection surface and convenient operation. It is one of the commonly used imaging diagnostic techniques in medicine [7]. With the increasing application of X-ray technology in medicine, medical image mosaic methods have become a research hotspot and difficulty in medical image processing [8, 9]. High-quality X-ray medical image mosaic is of great significance for preoperative diagnosis and intraoperative monitoring. Image mosaic technology is to apply a computer to match and align the overlapping images and finally synthesize a complete new image technology containing each image information [10]. It usually includes image acquisition, image registration, and image synthesis. Furthermore, image registration is the key to image mosaic. There are more image registration methods based on feature research. The scale-invariant feature transform (SIFT) algorithm is a commonly applied feature extraction and matching algorithm. It has good matching characteristics in image scaling and rotation transformation, with a good stability [11, 12]. SIFT is currently a research hotspot in image matching, and many mosaic algorithms are implemented based on SIFT. Therefore, the registration and splicing of X-ray images were implemented in this study under the registration method of feature points on the basis of SIFT, and the original algorithm was improved, so as to better realize the splicing of X-ray medical images. To sum up, it was necessary to investigate the effects of low-dose X-ray based on image mosaic algorithm on DNA damage in peripheral blood lymphocytes of patients with cardiovascular diseases, so as to provide reference for the evaluation of X-ray radiation damage in patients with cardiovascular intervention. Then, it was applied to the blood immune cell damage in patients with cardiovascular intervention, to explore the relationship between radiation dose and lymphocyte DNA damage, thereby providing a theoretical basis for interventional treatment of cardiovascular diseases.

2. Materials and Methods

2.1. Research Objects. From October 2017 to October 2020, 88 inpatients with cardiac interventional diagnosis and treatment in hospital were selected as the research objects, including 48 males and 40 females, with an average age of 60.26 ± 7.22 years. They were enrolled into group A (coronary artery intervention), group B (coronary angiography), group C (radiofrequency ablation), and group D (permanent cardiac pacemaker implantation) according to the interventional procedures. This experiment had been authorized by the Ethics Committee of the hospital, and the patients involved in the study knew and agreed.

2.2. Case Inclusion Criteria. The criteria for inclusion were defined to include patients who were 20–70 years old, underwent the interventional cardiovascular surgery, had the value of body mass index (BMI) of 17.9–$31.2 \, kg/m^2$, had basically normal functions of the heart, liver, kidney, and lung, received voluntary choice of interventional surgery, and had complete case data.

2.3. Case Exclusion Criteria. The criteria for exclusion were defined to include patients who suffered from abnormal coagulation function, had systemic metabolic diseases, suffered from organic dysfunction of the heart, liver, kidney, and lung, had diseases of the nervous or mental system, suffered from allergic constitution, had combination of other diseases affecting the test results, were pregnant or in the lactating period, and had incomplete clinical data.

2.4. Lymphocyte Separation Method. About $0.2 \, mL$ of the patient's peripheral blood was extracted and processed with anticoagulation by heparin. The precooled lymphocyte separation solution was added into the centrifuge tube, and the peripheral blood was added slowly along the inner wall of the centrifuge tube. Then, it was centrifuged at 3,500 rpm for 2 minutes. The off-white lymphocyte layer was transferred to a $2 \, mL$ centrifuge tube, and the phosphate buffer saline (PBS) was added into the tube. Next, it should be mixed well and centrifuged at 1,500 rpm for 6 minutes, and the supernatant was discarded. The cells were washed 3 times and resuspended by PBS. Besides, the cell concentration was adjusted to $2 \times 10^4/mL$, and the tube was placed in a refrigerator at $4°C$ and stored for later use.

2.5. Neutral Single-Cell Gel Electrophoresis. First, the gel was spread. The slide was placed in a 1% agarose solution. After taking it out, the slide was placed at $4°C$ for more than 1 hour until it was solidified. This was the first layer of gel. Then, $100 \, \mu L$ of 0.5% agarose was spread on the surface of the frosted glass slide and quickly covered with a cover glass for solidification at $4°C$. This was the second layer of gel. Besides, $160 \, \mu L$ of low-melting-temperature agarose with 0.5% ($37°C$) was mixed with the $20 \, \mu L$ of cell suspension thoroughly. Then, it was spread on the first layer of gel, covered with the cover glass, and cured, so that the spread of gel was finished, followed by cell lysis, and the slide was placed in the cell lysis solution overnight at $4°C$. After electrophoresis, the slide was set in the positive end of the electrophoresis tank and the freshly configured electrophoresis buffer was poured in the tank for 10–30 minutes, so that the DNA was melted. The voltage was set as 25 V, current was set as 240 mA, and there was electrophoresis for 30 minutes. After the electrophoresis was finished, the neutralization buffer solution was employed to soak and wash it 3 times (5 minutes each time). $20 \, \mu L$ of ethidium bromide was used for staining, and the results were observed under a fluorescence microscope. The emission wavelength was set to 590 nm, and the excitation wavelength was 520 nm. Intact cells presented with round fluorescent core, comet head, and no tail. Damaged cells

manifested as follows. Comet tails extended towards the anode, with bright head and tail. 100 cells were selected from each sample and analyzed by comet assay software project (CASP) to obtain TDNA and TM. Moreover, the larger the values, the more serious the DNA damage.

2.6. Low-Dose X-Ray Algorithm Based on Image Mosaic. Image mosaic referred to the process of overlapping information image sequences of the same scene at different times or perspectives. Image mosaic usually included image information acquisition, image preprocessing, registration and image information fusion, and postprocessing. At present, the commonly used method of image mosaic has been feature detection and matching based on invariant technology. The speeded up robust feature (SURF) detection algorithm was an accelerated and enhanced version of SIFT feature detection algorithm.

SURF was substantially featured with rotation, translation, zooming, and obtaining speed. For the integral graph $P(x, y)$, the calculation equation of the integral image was as follows:

$$I_\Sigma(P) = \sum_{i=0}^{i<x} \sum_{j=0}^{i<y} I(i, j), \tag{1}$$

where $I(i, j)$ stood for the pixel value and $I_\Sigma(P)$ represented the integral image.

The pixels in the S area of the original image could be expressed as follows:

$$S = A - B - C + D. \tag{2}$$

SURF could keep the calculation time constant while changing the image size and could accelerate the convolution process between the box filters of different sizes and the original image. SURF extracted the key points mainly based on the scale space theory. The first was to generate the scale space pyramid. When SURF constructed the scale space pyramid, the second-order Gaussian kernel function was adopted to approximately substitute the SIFT process, and the integral image was employed during convolution. The next step was to determine the candidate extreme points. The SIFT local extreme value discrimination applied the det (H) value of the Hessian matrix determinant. Furthermore, SURF employed an estimated value that approximated det (H) to express ΔH that could be calculated as follows:

$$\Delta H = D_{xx}D_{yy} - (0.9D_{xy})^2. \tag{3}$$

If ΔH was positive, it indicated that the point was a maximum or minimum point. Afterwards, there was non-maximum suppression in a $3 \times 3 \times 3$ stereoscopic neighborhood to obtain the candidate extreme value, and the position and size of the candidate extreme value were recorded. Finally, there was the operation to eliminate unstable points.

The main direction of SURF key points was determined by calculating Haar wavelet characteristics in the key-point area. First, the sum of the horizontal features and vertical

Haar wavelet features of all key points in the 60-degree sector in the neighborhood was statistically analyzed, and they were rotated at a certain interval. Thus, the maximum fan direction was the main direction of the key points. After the main direction was determined, the generated feature point descriptor was confirmed, and a square frame with a side length of 20 N around the key point was selected and divided into 16 subregions. 25-pixel Haar wavelet features in the X and Y directions were calculated in each subregion. Finally, there was feature matching. The initial judgment of the trace of the Hessian matrix was used, and then the Euclidean distance was used for the measurement. The calculation equation for the similarity measure of the two feature point descriptors was as follows:

$$D = \left[\sum_{k=0}^{k=n} \left(X_{ik} - X_{jk}\right)^2\right]^{(1/2)}, \tag{4}$$

where n expressed the dimension of the feature vector; X_{ik} stood for the k-th element of the i-th feature descriptor in the image to be registered; and X_{jk} stood for the k-th element of the j-th feature descriptor in the standard image.

2.7. Observation Indicators. The peripheral venous blood of all patients was collected before and 24 hours after surgery. Neutral single-cell gel electrophoresis was applied to detect the lymphocyte DNA damage indicators of the patients. The DNA damage indicators included the TDNA and TM. The interventional equipment was FD 10 digital subtraction angiography (DSA), produced by Philips. In addition, the radiation-dose parameters of all patients were recorded in real time, including CD and DAP, and the relationship between radiation dose and DNA damage effects was analyzed.

2.8. Statistical Analysis. SPSS20.0 statistical software was used for analysis, and the measurement data were expressed as mean ± standard deviation ($\overline{x} \pm s$). The t-test was used for comparison between the two groups, and the analysis of variance was used for comparison among multiple groups. Besides, the count data were presented as percentage (%), and χ^2 test was used for comparison between groups. In addition, $P < 0.05$ meant that the difference between groups was statistically substantial.

3. Results

3.1. Low-Dose X-Ray Image Quality Evaluation Based on Image Mosaic Algorithm. The information entropy and absolute mean brightness error (AMBE) evaluation indicators were applied to evaluate the image mosaic quality. The original image was set as $x(i, j)$, and the processed image was set as $y(i, j)$; both of them had $LM \times N$ gray levels, so the gray distribution density of the processed image could be expressed as follows:

$$\begin{cases} \rho(x) = \rho\{L = x\}, & x \in L, \\ \text{AMBE} = M(X) - M(Y). \end{cases} \tag{5}$$

Furthermore, the expression of information entropy and AMBE was shown in (6) and (7) in turn.

$$H(x) = -\sum_{x \in L} p(x)\log_2 p(x), \tag{6}$$

$$\text{AMBE} = M(X) - M(Y), \tag{7}$$

where $M(X)$ and $M(Y)$ were the average gray values of the original and processed images, respectively. Moreover, the larger the information entropy value, the more the information in the image and the higher the image quality. The greater the AMBE, the larger the average brightness error of the original and processed images.

The X-ray image processing results of different image mosaic and segmentation algorithms are shown in Figures 1–3. These figures, respectively, showed the comparison results of entropy (H), AMBE value, and X-ray images of patients in each group treated by different algorithms. The AMBE and information entropy values of the algorithm in this study were 0.0624 and 7.0364 in sequence. The X-ray image mosaic algorithm proposed in this study not only could effectively realize image mosaic but also was superior to traditional SIFT methods in terms of image mosaic quality.

3.2. Comparison of the General Data of all Patients. The comparison results of the general data of patients in each group are shown in Figures 4–7. Figure 4 indicates that the average age of patients in groups A, B, C, and D was 62.84 ± 4.79 years, 63.65 ± 5.76 years, 62.74 ± 4.39 years, and 63.64 ± 5.04 years in turn. It was found from Figure 5 that the proportion of hypertension in patients from group A was 58.4%, the proportion of that from group B was 60.3%, the proportion of that from group C was 57.2, and the proportion of that from group D was 61.2%. There were 58.4% of patients with hyperlipidemia in group A, 60.3% of those in group B, 57.2% of those in group C, and 61.2% of those in group D (Figure 6). In Figure 7, the proportion of patients who suffered from diabetes in group A was 58.4%, the proportion of patients who suffered from diabetes in group B was 60.3%, the proportion of patients who suffered from diabetes in group C was 57.2, and the proportion of patients who suffered from diabetes in group D was 61.2%. There was no statistical significance in age, proportion of patients with hypertension, hyperlipidemia, and diabetes between the two groups ($P > 0.05$).

3.3. Comparison of Radiation Dose of Patients from Each Group. The radiation-dose results of patients in the four groups are shown in Figures 8 and 9. It disclosed that the CD values of patients from groups A, B, C, and D were 0.38 ± 0.08 Gy, 0.77 ± 0.16 Gy, 0.93 ± 0.23 Gy, and 1.37 ± 0.21 Gy, respectively. In addition, the DAP values of patients from groups A, B, C, and D were 0.38 ± 0.08 Gy/cm^2, 0.77 ± 0.16 Gy/cm^2, 0.93 ± 0.23 Gy/cm^2, and 1.37 ± 0.21 Gy/cm^2. Therefore, the CD and DAP of patients from group A were the lowest while those of group D were the highest. Besides, the CD and DAP values of patients from group D were obviously higher than the values of groups A, B, and C ($P < 0.05$).

3.4. Comparison of DNA Damage Indicators of Patients from Each Group. Figure 10 indicates the comparison results of TDNA in patients from each group before and 24 hours after surgery. The preoperative TDNA of patients from groups A, B, C, and D was $3.22 \pm 1.98\%$, $3.08 \pm 2.21\%$, $2.97 \pm 2.01\%$, $2.77 \pm 1.52\%$, respectively. However, TDNA of patients in groups A, B, C, and D 24 hours after surgery was $13.76 \pm 2.65\%$, $19.53 \pm 2.12\%$, $21.87 \pm 2.41\%$, and $29.13 \pm 2.54\%$ in turn. Compared with before surgery, the TDNA of patients from the 4 groups rose substantially ($P < 0.01$), and the TDNA of group D was obviously higher than that of the other three groups ($P < 0.01$) 24 hours after surgery.

Figure 11 indicates the comparison results of TM values in patients from each group before and 24 hours after surgery. The preoperative TM of patients from groups A, B, C, and D was 0.35 ± 0.21, 0.54 ± 0.38, 0.45 ± 0.29, and 0.32 ± 0.27, respectively, while the 24-hour postoperative TM of groups A, B, C, and D was 11.85 ± 1.38, 19.76 ± 2.87, 22.36 ± 2.62, and 34.86 ± 4.54 in sequence. Above all, the values of TM in patients from the four groups before surgery were dramatically higher than the values 24 hours after surgery ($P < 0.01$). Furthermore, the values of TM in patients of group D before surgery elevated hugely in contrast to the values 24 hours after surgery ($P < 0.01$).

3.5. Regression Analysis Results. The radiation dose (CD and DAP) and the DNA damage indicators (TM and TDNA) were used for regression analysis, and its results are shown in Table 1. It suggested that the CD, DAP, TM, and TDNA of the patients in this study were all showing a positive correlation ($P < 0.01$), indicating that the radiation dose was positively related to the degree of DNA damage. Furthermore, the greater the radiation dose, the more serious the DNA damage. The correlation coefficients between radiation dose (CD and DAP) and DNA damage indicators (TM and TDNA%) are shown in Table 1.

4. Discussion

In recent years, image mosaic technology has become the focus of research in medical image processing. The research of Lv and Wen [13] has pointed out that high-quality X-ray medical image mosaic uses computers to match and align overlapping images, which is of great significance for preoperative diagnosis and intraoperative monitoring. Based on the traditional SIFT algorithm, the mosaic offset was obtained in this study through feature point detection and registration operations, and finally, the X-ray image mosaic process was completed. It showed that the X-ray image mosaic algorithm proposed in this study not only could effectively realize image mosaic but also was better than
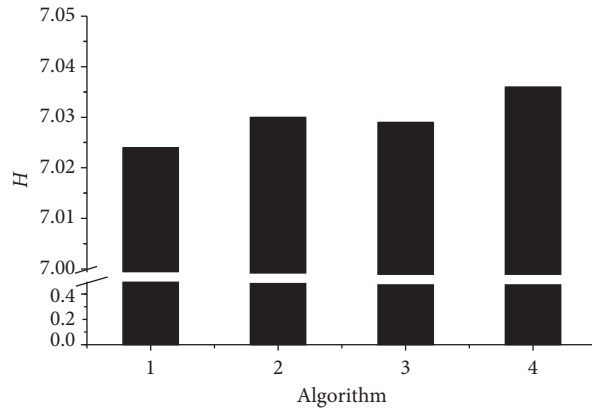
FIGURE 1: Comparison of information entropy values of different algorithms (note: 1, 2, 3, and 4 stood for the original algorithm, the eight-direction Sobel, the improved eight-direction Sobel, and the algorithm proposed in this study, respectively).
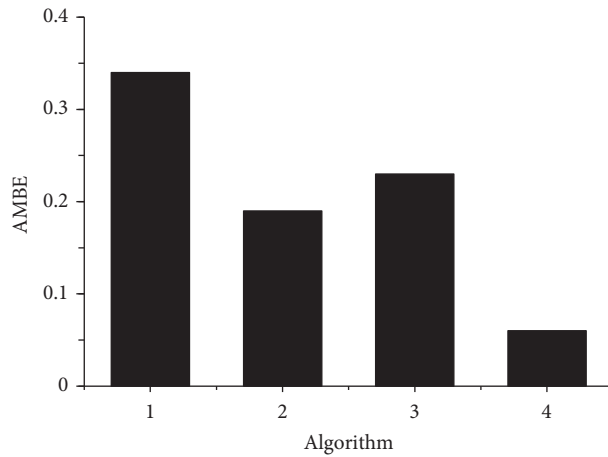

FIGURE 2: Comparison of AMBE values of the four different algorithms (note: 1 expressed the original algorithm; 2 represented the eight-direction Sobel; 3 stood for the improved eight-direction Sobel; and 4 was the algorithm in this study).
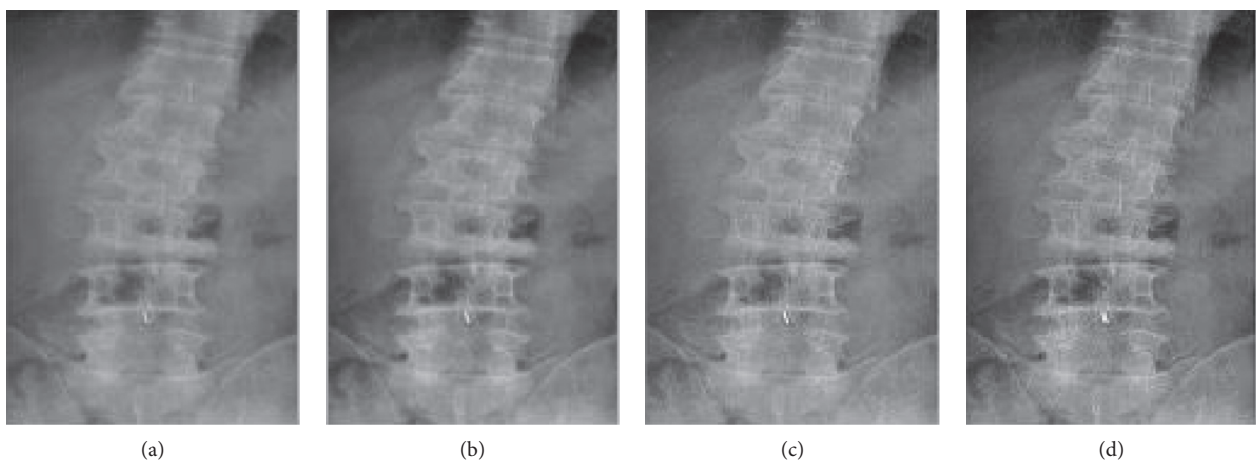
FIGURE 3: X-ray images of a patient. (a) Original algorithm. (b) Eight-direction Sobel. (c) The improved eight-direction Sobel. (d) The algorithm in this study.

traditional SIFT method in terms of image mosaic quality. This was consistent with the research results of Zhao et al. [14].

Lymphocytes are relatively sensitive to X-ray ionizing radiation and are extensively distributed in the human body. Therefore, lymphocytes are very suitable as a sample of
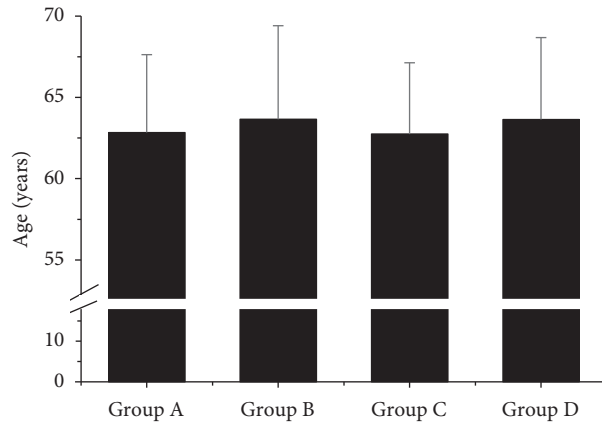
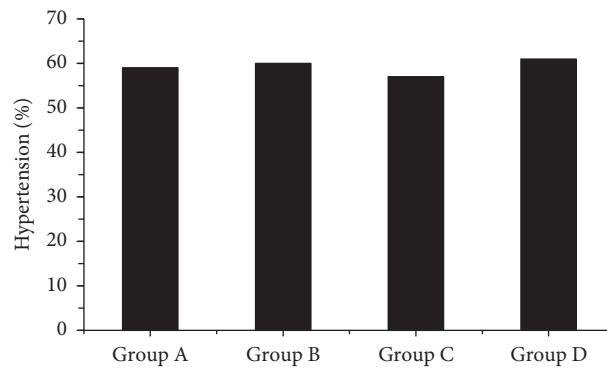FIGURE 4: Comparison of the age of patients in each group.

FIGURE 5: Comparison of the proportion of patients with hypertension in each group.
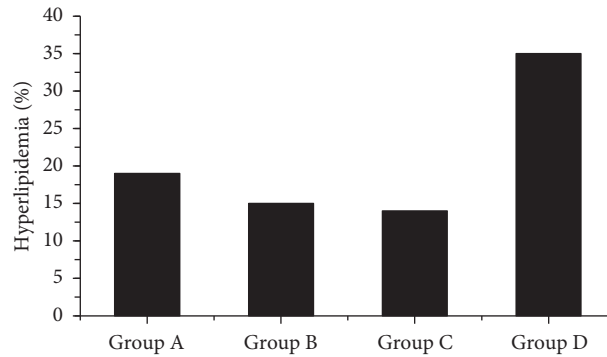

FIGURE 6: Comparison of the proportion of patients with hyperlipidemia in each group.
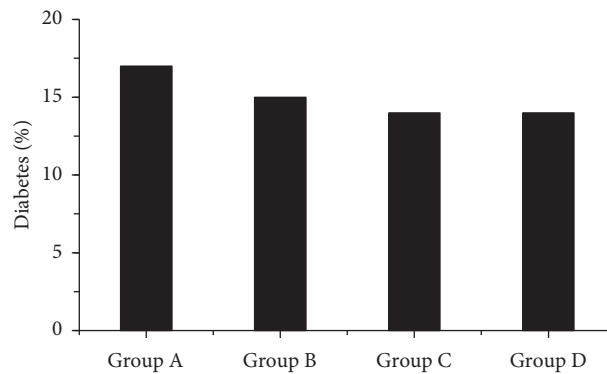

FIGURE 7: Comparison of the proportion of patients suffering from diabetes in each group.
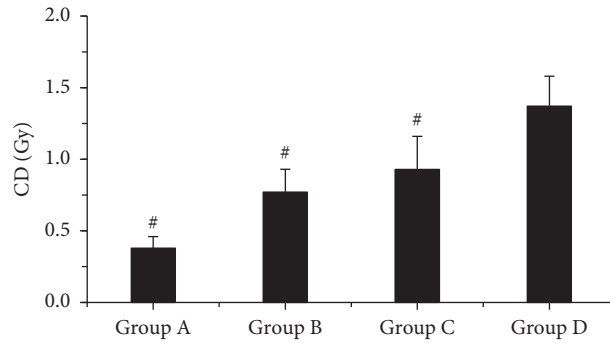
FIGURE 8: Comparison of the CD values of patients in each group (note: # indicated that the difference was statistically substantial compared with group D ($P < 0.05$)).
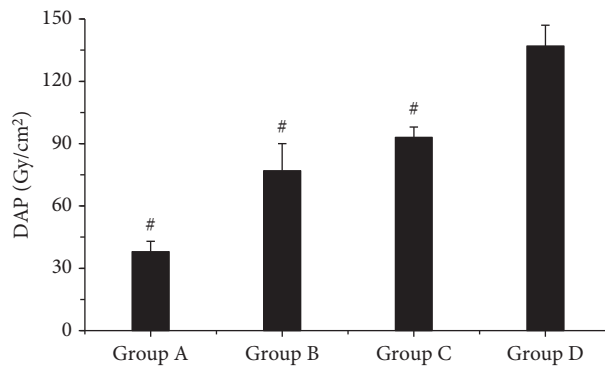

FIGURE 9: Comparison of the DAP values of patients from groups A, B, C, and D (# meant that there was a statistically remarkable difference in contrast to group D ($P < 0.05$)).
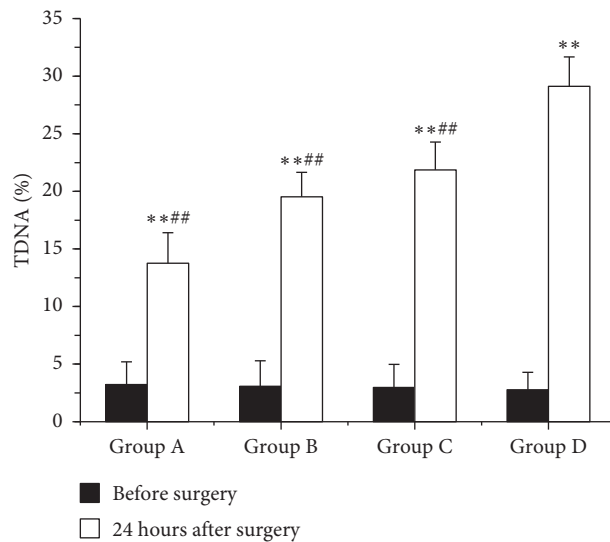

FIGURE 10: Comparison of TDNA values of patients in each group (note: ∗∗ showed that the difference was statistically obvious compared to before surgery ($P < 0.01$) and ## revealed that the difference was statistically marked in contrast to group D ($P < 0.01$)).

radiation damage research, which can more accurately reflect the degree of radiation damage to the entire body [15]. In addition, the extraction of peripheral venous blood lymphocytes, combined with single-cell gel electrophoresis technology, can extremely promote the efficiency of acute radiation injury research. The results of this study found that the CD values of patients from groups A, B, C, and D were 0.38 ± 0.08 Gy, 0.77 ± 0.16 Gy, 0.93 ± 0.23 Gy, and 1.37 ± 0.21 Gy in turn, and the DAP values of each group were 0.38 ± 0.08 Gy/cm^2, 0.77 ± 0.16 Gy/cm^2, 0.93 ± 0.23 Gy/cm^2, and 1.37 ± 0.21 Gy/cm^2, respectively. Thus, the CD and DAP value of group A was the lowest, while the values of
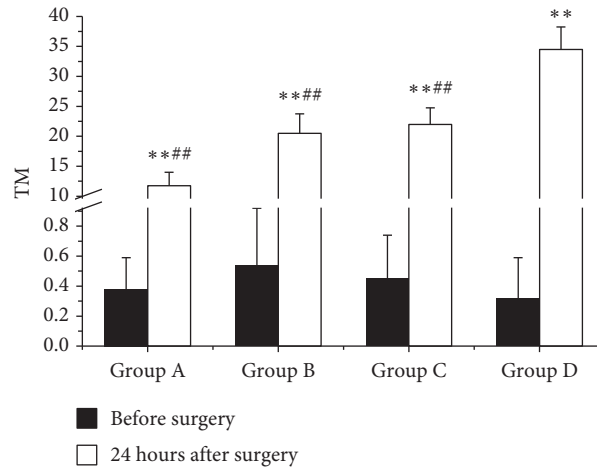
FIGURE 11: Comparison of TM values of patients in each group (note: ∗∗ showed that there was a statistically obvious difference compared with before surgery ($P < 0.01$) and ## revealed that there was a statistically substantial difference in contrast to group D ($P < 0.01$)).

TABLE 1: Regression analysis results of radiation dose (CD and DAP) and DNA damage indicators (TM and TDNA).

	TDNA	TM	CD	DAP
TDNA	—			
TM	0.985	—		
CD	0.968	0.985	—	
DAP	0.981	0.992	0.982	—

group D were the highest. Besides, the CD and DAP values of patients from group D rose markedly in contrast to the values of group A, B, and C ($P < 0.05$). This was in line with the research results of Rawojć et al. [16]. Through the above results, there were obvious differences in the radiation dose of patients from each group. Then, the TDNA and TM were applied to assess the DNA damage effect, finding that the TDNA and TM values of patients from the four groups were markedly higher than those before the surgery ($P < 0.01$). Furthermore, the TDNA and TM of group D were hugely higher than those of groups A, B, and C 24 hours after surgery ($P < 0.01$). The results of regression analysis revealed that the CD, DAP, TM, and TDNA of all patients presented a positive correlation ($P < 0.01$), indicating that the radiation dose was positively associated with the degree of DNA damage. Moreover, the greater the radiation dose, the more serious the DNA damage. In this study, the neutral single-cell gel electrophoresis method was used for detection, which mainly detected the breaking of DNA double strands, with high specificity. Compared with other parameters, and TM and TDNA had a higher correlation with the degree of DNA damage and were more sensitive and accurate [17, 18]. According to the research of Chen et al. [19], although many mosaic algorithms are implemented based on SIFT algorithm, radiation damage suffered by cardiovascular intervention patients is generally acute radiation damage. DNA can continuously repair itself. Therefore, the biological effects in the short term cannot reflect the final genetic damage status. For further research on the long-term health risk assessment of radiation for patients, a large number of long-term follow-up studies are also needed. In addition, there are still a lot of uncertainties in the evaluation of radiation damage through single-cell gel electrophoresis technology, and the standardized laboratory standards need to be established.

5. Conclusion

IMA was employed to enhance the quality of low-dose X-ray images and applied to the analysis of DNA damage in peripheral blood lymphocytes of cardiovascular patients. It was found that the quality of low-dose X-ray images based on IMA was obviously improved. Radiation dose (DAP and CD) values were substantially positively correlated with TDNA and TM values of peripheral blood lymphocyte DNA damage indicators of cardiovascular patients ($P < 0.01$). It indicated that X-ray radiotherapy based on IMA caused a certain damage on peripheral blood lymphocytes of cardiovascular patients, and the greater the radiation dose, the more serious the DNA damage. However, there are still some shortcomings in this research. For example, the number of samples is limited, the number of samples should be increased in the future, and the time range of detection indicators can be further refined. In short, the results of this study can provide a reference basis for X-ray radiation damage assessment of patients with cardiovascular intervention surgeries.

Data Availability

No data were used to support this study.

Conflicts of Interest

The authors declare that they have no conflicts of interest.

Acknowledgments

References

[1] S. A. Romero, C. T. Minson, and J. R. Halliwill, "The cardiovascular system after exercise," *Journal of Applied Physiology*, vol. 122, no. 4, pp. 925–932, 2017.

[2] J. P. Garcia, A. Santana, D. L. Baruqui et al., "The cardiovascular effects of chocolate," *Reviews in Cardiovascular Medicine*, vol. 19, no. 4, pp. 123–127, 2018.

[3] A. Oesterle, U. Laufs, and J. K. Liao, "Pleiotropic Effects of statins on the cardiovascular system," *Circulation Research*, vol. 120, no. 1, pp. 229–243, 2017.

[4] H. J. Jenkins, A. S. Downie, C. S. Moore, and D. F. Simon, "Current evidence for spinal X-ray use in the chiropractic profession: a narrative review," *Chiropractic and Manual Therapies*, vol. 26, 2018.

[5] W. Yashiro, "Hard X-ray imaging microscopy with self-imaging phenomenon," *Microscopy*, vol. 67, no. 6, pp. 303–316, 2018.

[6] J. A. Kochan, M. van den Belt, J. von der Lippe et al., "Ultrasoft X-ray system for imaging the early cellular responses to X-ray induced DNA damage," *Nucleic Acids Research*, vol. 47, no. 17, 2019.

[7] E. F. Garman and M. Weik, "X-ray radiation damage to biological samples: recent progress," *Journal of Synchrotron Radiation*, vol. 26, no. 4, pp. 907–911, 2019.

[8] F. Yang, Y. He, Z. S. Deng et al., "Improvement of automated image stitching system for DR X-ray images," *Computers in Biology and Medicine*, vol. 71, pp. 108–114, 2016.

[9] J. Wang, X. Zhang, Z. Sun et al., "An efficient intensity-based ready-to-use X-ray image stitcher," *Int J Med Robot*, vol. 14, no. 5, Article ID e1925, 2018.

[10] O. Svystun, A. Wenzel, L. Schropp et al., "Image-stitching artefacts and distortion in CCD-based cephalograms and their association with sensor type and head movement: *ex vivo* study," *Dentomaxillofacial Radiology*, vol. 49, no. 3, Article ID 20190315, 2020.

[11] R. Vaser, S. Adusumalli, S. N. Leng et al., "SIFT missense predictions for genomes," *Nature Protocols*, vol. 11, no. 1, pp. 1–9, 2016.

[12] D. H. Lee, D. W. Lee, and B. S. Han, "Possibility study of scale invariant feature transform (SIFT) algorithm application to spine magnetic resonance imaging," *PLoS One*, vol. 11, no. 4, Article ID e0153043, 2016.

[13] Z. Lv and X. Wen, "Interaction of edge-cloud computing based on SDN and NFV for next generation IoT," *IEEE Internet of Things Journal*, vol. 10, Article ID 2942719, 2019.

[14] H. Zhao, N. Chen, T. Li et al., "Motion correction in optical resolution photoacoustic microscopy," *IEEE Transactions on Medical Imaging*, vol. 38, no. 9, pp. 2139–2150, 2019.

[15] E. Tran, P. F. Robbins, Y. C. Lu et al., "T-cell transfer therapy targeting mutant KRAS in cancer," *New England Journal of Medicine*, vol. 375, no. 23, pp. 2255–2262, 2016.

[16] K. Rawojć, J. Miszczyk, A. Możdżeń et al., "Evaluation of the premature chromosome condensation scoring protocol after proton and X-ray irradiation of human peripheral blood lymphocytes at high doses range," *International Journal of Radiation Biology*, vol. 94, no. 11, pp. 996–1005, 2018.

[17] M. A. Bhat and G. Gandhi, "Assessment of DNA damage in leukocytes of patients with coronary artery disease by comet assay," *International Heart Journal*, vol. 58, no. 2, pp. 271–274, 2017.

[18] K. Zhang, L. Wang, S. Si et al., "Crocin improves the proliferation and cytotoxic function of T cells in children with acute lymphoblastic leukemia," *Biomedicine & Pharmacotherapy*, vol. 99, pp. 96–100, 2018.

[19] Y. Chen, S. J. Hu, H. Mao et al., "Application of the best evacuation model of deep learning in the design of public structures," *Image and Vision Computing*, vol. 102, Article ID 103975, 2020.